Reduction of blurring in broadband volume holographic imaging using a deconvolution method

YANLU LV,[1] XUANXUAN ZHANG,[1] DONG ZHANG,[1] LIN ZHANG,[1] YUAN LUO,[2] AND JIANWEN LUO[1,3,*]

[1]*Department of Biomedical Engineering, School of Medicine, Tsinghua University, Beijing 100084, China*
[2]*Institute of Medical Device and Imaging, National Taiwan University, Taipei 10051, Taiwan*
[3]*Center for Biomedical Imaging Research, Tsinghua University, Beijing 100084, China*
[*]luo_jianwen@tsinghua.edu.cn

Abstract: Volume holographic imaging (VHI) is a promising biomedical imaging tool that can simultaneously provide multi-depth or multispectral information. When a VHI system is probed with a broadband source, the intensity spreads in the horizontal direction, causing degradation of the image contrast. We theoretically analyzed the reason of the horizontal intensity spread, and the analysis was validated by the simulation and experimental results of the broadband impulse response of the VHI system. We proposed a deconvolution method to reduce the horizontal intensity spread and increase the image contrast. Imaging experiments with three different objects, including bright field illuminated USAF test target and lung tissue specimen and fluorescent beads, were carried out to test the performance of the proposed method. The results demonstrated that the proposed method can significantly improve the horizontal contrast of the image acquire by broadband VHI system.

References and links

1. A. Sinha and G. Barbastathis. "Volume holographic imaging for surface metrology at long working distances," Opt. Express **11**(24), 3202–3209 (2003).
2. W. Liu, G. Barbastathis, and D. Psaltis. "Volume holographic hyperspectral imaging," Appl. Opt. **43**(18), 3581–3599 (2004).
3. Y. Lv, J. Zhang, F. Liu, J. Shi, H. Guang, J. Bai, and J. Luo. "Spectral selective fluorescence molecular imaging with volume holographic imaging system," J. Innov. Opt. Heal. Sci. **09**(5), 1650010 (2016).
4. Y. Luo, P. J. Gelsinger-Austin, J. M. Watson, G. Barbastathis, J. K. Barton, and R. K. Kostuk. "Laser-induced fluorescence imaging of subsurface tissue structures with a volume holographic spatial-spectral imaging system," Opt. Lett. **33**(18), 2098-100 (2008).
5. C. Y. Lin, W. T. Lin, H. H. Chen, J. M. Wong, V. R. Singh, and Y. Luo. "Talbot multi-focal holographic fluorescence endoscopy for optically sectioned imaging," Opt. Lett. **41**(2), 344 (2016).
6. W. Liu, D. Psaltis, and G. Barbastathis. "Real-time spectral imaging in three spatial dimensions," Opt. Lett. **27**(10), 854–856 (2002).
7. A. Sinha and G. Barbastathis. "Broadband volume holographic imaging," Appl. Opt. **43**(27), 5214–5221 (2004).
8. W. Sun and G. Barbastathis. "Rainbow volume holographic imaging," Opt. Lett. **30**(9), 976–978 (2005).
9. E. E. de Leon, J. W. Brownlee, P. Gelsinger-Austin, and R. K. Kostuk. "Dual-grating confocal-rainbow volume holographic imaging system designs for high depth resolution," Appl. Opt. **51**(29), 6952–6961 (2012).
10. Y. Lv, J. Zhang, D. Zhang, W. Cai, N. Chen, and J. Luo. "In vivo simultaneous multispectral fluorescence imaging with spectral multiplexed volume holographic imaging system," J. Biomed Opt. **21**(6), 060502 (2016).
11. D. Walter, A. Liu, E. Franklin, D. Macdonald, B. Mitchell, and T. Trupke. "Contrast enhancement of luminescence images via point-spread deconvolution," in Proceedings of IEEE Photovoltaic Specialists Conference (PVSC) (IEEE, 2012), pp. 307–312.
12. H. H. Chen, S. B. Oh, X. Zhai, J. C. Tsai, L. C. Cao, G. Barbastathis, and Y. Luo. "Wigner analysis of three dimensional pupil with finite lateral aperture," Opt. Express **23**(4), 4046–4054 (2015).
13. Se Baek Oh. "Volume holographic pupils in ray, wave, statistical optics, and wigner space," Ph.D. dissertation (Massachusetts Institute of Technology, 2009).
14. P. Wissmann, Se Baek Oh, and G. Barbastathis. "Simulation and optimization of volume holographic imaging systems in zemax," Opt. Express **16**(10), 7516–7524 (2008).

15. P. Günter, J. Huignard, and G. Barbastathis. "The transfer function of volume holographic optical systems," in *Photorefractive Materials and Their Applications 3*, Fellows H. E. (Springer, 2007).
16. J. M. Castro, J. Brownlee, Y. Luo, E. de Leon, J. K. Barton, G. Barbastathis, and R. K. Kostuk. "Spatial spectral volume holographic systems: resolution dependence on effective thickness," Appl. Opt. **50**(7), 1038–1046 (2011).
17. N. Cohen, S. Yang, A. Andalman, M. Broxton, L. Grosenick, K. Deisseroth, M. Horowitz, and M. Levoy. "Enhancing the performance of the light field microscope using wavefront coding," Opt. Express **22**(20), 24817–24839 (2014).
18. P. C. Hansen, J. G. Nagy, and D. P. O'Leary. *Deblurring Images: Matrices, Spectra, and Filtering* (SIAM, 2006).
19. J. Shi, F. Liu, H. Pu, S. Zuo, J. Luo, and J. Bai. "An adaptive support driven reweighted l1-regularization algorithm for fluorescence molecular tomography," Biomed. Opt. Express **5**(11), 4039–4052 (2014).
20. B. Amizic, L. Spinoulas, R. Molina, and A. K. Katsaggelos. "Compressive blind image deconvolution," IEEE Transactions on Image Processing A Publication of the IEEE Signal Processing Society **22**(10), 3994–4006 (2013).
21. B. A. Scalettar, J. R. Swedlow, J. W. Sedat, and D. A. Agard, "Dispersion, aberration and deconvolution in multi-wavelength fluorescence images," J. Microsc-Oxford **182**(Pt 1), 50–60 (1996).
22. H. Yang, Y. Chiao, P. Huang, and S. Lai. "Blind image deblurring with modified richardson-lucy deconvolution for ringing artifact suppression," in Proceedings of Advances in Image and Video Technology - Pacific Rim Symposium, Y. Ho, (Springer, 2011), pp. 240–251.

1. Introduction

A volume holographic grating (VHG) is a three-dimensional (3D) optical element that has been successfully applied to microscopic and spectroscopic applications, such as depth selective imaging [1], tunable multispectral and hyperspectral imaging [2, 3], and non-scanning 3D fluorescence microscopy [4,5]. In these volume holographic imaging (VHI) systems, the gratings are formed by exposure of a thick photo-sensitive material to the interference of two or more mutually coherent wave-fronts and placed on the Fourier plane of a $4f$ imaging system to obtain image of biological samples. By exploiting the shift variance due to Bragg condition, the VHI system exhibits the capability of simultaneously acquiring spatial images with horizontal-dependent spectral information under broadband illumination [6]. With broadband illumination, the VHI system achieves improved field of view (FOV) but reduced depth resolution. Sinha et al. discussed the relationship between the depth resolution and the bandwidth [7]. They verified that when the system is used to image reflective object illuminated with a broadband source, there is a performance trade-off between the FOV and the contrast between surfaces at different depths. To mitigate this problem of decreased depth resolution, active illumination approaches with additional dispersion components in the illumination path were utilized [8,9]. However, these methods require careful design and skillful optical elements alignment techniques to minimize the noise caused by specular reflection. In addition, the performance of these methods can be decreased in passive biomedical fluorescence imaging applications, where the intensity and the optical scattering property of the tissue make aligning the dispersion components in fluorescence detection path much more challenging.

In our following imaging experiments with $4f$ VHI system, we find that the illumination bandwidth can also affect the lateral image contrast of the object without surface features. Broadband illumination imaging, such as white light and fluorescence, is widely used in many biomedical applications. When the imaging object emits fluorescence or scatters broadband light, the contrast of the image acquired with VHI system deteriorates in the horizontal direction [10], which can have noticeable effect on the diagnosis of disease. Therefore, a better understanding of the imaging performance of volume holograms under broadband illumination is necessary to optimize the construction of VHI system for various biomedical applications. Here, we presented the theoretical analysis of the system performance relating to the lateral contrast and bandwidth of the illumination and we explained the reason why it is possible to use deconvolution [11], a common method for shift invariance imaging systems, to improve the contrast of the images acquired by VHI system, which is not shift invariant [12]. Then we experimentally demonstrated the contrast improvement in the applications of imaging both broadband illuminated objects and fluorescent objects with the deconvolution method. We also analyzed the relationship between

the structure parameters of the broadband VHI system and the size of the horizontal intensity spread on the image plane, and our data suggests a general design principle for controlling the size of the horizontal intensity spread while meeting the imaging requirement.

The paper is organized as follows. In Section 2, the geometry of the VHI system and the k-sphere representation of Bragg matched condition and Bragg degeneracy are revisited. In Section 3, the model of the impulse response of the broadband VHI system is described. In Section 4, the experimental results of imaging both broadband illuminated object and fluorescent object are presented. The consistency and accuracy of the images obtained with the deconvolution method are investigated. In Section 5, the relationship between the structure parameters of the broadband VHI system and the size of the horizontal intensity spread is investigated, the advantages and limitation of the deconvolution method are discussed, and some improvements to be done in the near future focusing on optimization of the deconvolution method are addressed.

2. Background

For simplicity, we assume that the VHG is unslanted and recorded by two planner waves with an inter-beam angle. In Fig. 1, the recording and readout procedure for planner VHG are illustrated with the k-sphere diagrams [13,14]. As shown in Fig. 1(a), the VHG is recorded within the photo-sensitive material by two mutually coherent plane waves with the inter-beam angles $\theta_r = \theta_s$. The wavelengths of the recording and probe waves are denoted as λ_f and λ_p, respectively. The wave-vectors of the signal beam, reference beam and probe beam are denoted as $|\mathbf{k}_s| = |\mathbf{k}_r| = 2\pi/\lambda_f$, and $|\mathbf{k}_p| = 2\pi/\lambda_p$, respectively. The grating vector $\mathbf{K}_g$ is then obtained as

$$\mathbf{K}_g = \mathbf{k}_s - \mathbf{k}_r, \tag{1}$$

When the prerecorded VHG with a grating vector $\mathbf{K}_g$ is probed by a plane wave, the efficiency of the diffraction wave is determined by the Bragg matched degree between $\mathbf{k}_p + \mathbf{K}_g$ and $\mathbf{k}_d$, i.e. $\delta\mathbf{k}_d = \mathbf{k}_p + \mathbf{K}_g - \mathbf{k}_d$. If they are fully Bragg matched and $\delta\mathbf{k}_d = 0$, the diffraction efficiency can achieve its peak value, whereas if $\delta\mathbf{k}_d \neq 0$, the diffraction efficiency decreases as the magnitude of $\delta\mathbf{k}_d$ increases (Figs. 1(b) and (c)) [13]. And this leads to the angle-spectral selectivity of the VHG. Another important property named Bragg wavelength degeneracy is shown in Fig. 1(d). For a single grating vector $\mathbf{K}_g$, the Bragg matched condition can be satisfied by an infinite number of combinations of probe wavelength $\mathbf{k}_p$ and incident angles. The Bragg selectivity and degeneracy property permit the VHG to work as a 3D Fourier filter with its unique angular-spectral filtering and imaging functions [5, 14, 15].

The basic geometry of a standard VHI system consisting of a $4f$ system and a VHG placed on the Fourier plane is shown in Fig. 2. An objective lens of focal lens f_1 is placed in front of the VHG to collimate the beam emitting from the point source on the object plane. The VHG has a finite aperture width of a and thickness of L. Because of the angular-spectral selectivity, when this system is illuminated with a monochromatic source, the VHG selectively diffracts the Bragg matched wave-front, which originates from the scattering object.

As shown in Fig. 1(d), when the probe wavelength is different from the recording one, the Bragg condition can be satisfied by tilting the direction of probe beam by an amount of $\delta\theta$, and each tilting angle requires a displacement of the probe point source along the x direction in the geometry shown in Fig. 2 [7]. When the VHI system is probed by a broadband illumination, different object slits can be mapped directly onto specific locations of the detector containing a unique spectral component determined by the Bragg degeneration, rather than only one slit image on the detector under a monochromatic illumination. As a result, the FOV of the VHI system is improved with the broadband illumination.
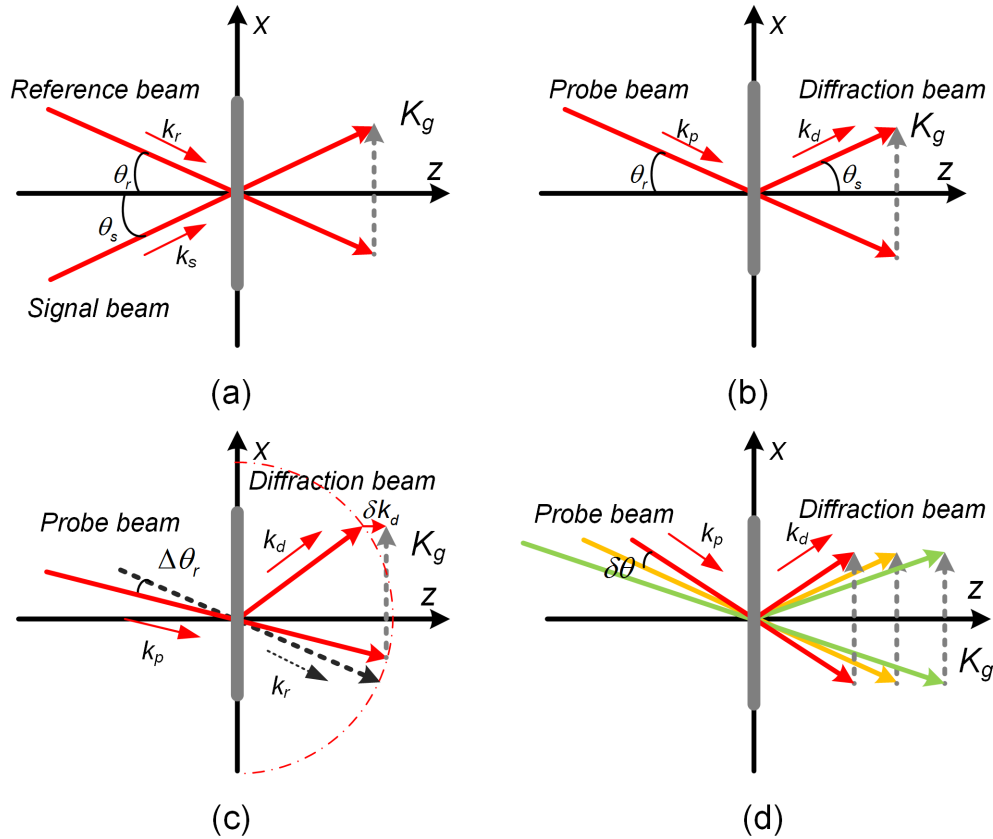
Fig. 1. The k-sphere diagrams for procedures of recording and readout VHG. (a) Two coherent plane waves interfere within the material and the recorded 3D interference pattern within the volume works as a 3D Fourier filter. (b) The VHG can be Bragg matched when the probe wave-vector coincides with the reference wave-vector in (a). (c) When the direction of the probe vector deviates $\Delta\theta_r$ from the reference vector, the Bragg matched condition is not satisfied, although the diffraction field can still be obtained. The diffraction efficiency is affected by the magnitude of the mismatch vector $\delta\mathbf{k}_d$. (d) For a grating vector, $\mathbf{K}_g$ can be Bragg matched with different pairs of wave-vector with corresponding tilting angles.

3. Deconvolution of the broadband VHI

3.1. Analysis of the broadband effect on the image contrast

The mechanism for the depth selectivity degradation under broadband illumination has been analyzed qualitatively for the 3D Fourier filter used in the VHI system [7]. When the surface featured object is illuminated with broadband source, spectrums at the defocus position can still be diffracted by the VHG, and the total diffracted energy of the spectral components is comparable to that at the focus position. However, when the focused surface-featureless object scattering or emitting broadband light is imaged with the VHI system, the image contrast in the horizontal direction suffers (marked with dashed rectangles in Figs. 3(a) and (b)) while the contrast in the vertical direction is less affected (Figs. 3(c) and (d)). The local contrast is calculated as

$$C_{thr} = \frac{I_{max} - I_{min}}{I_{max} + I_{min}}, \tag{2}$$
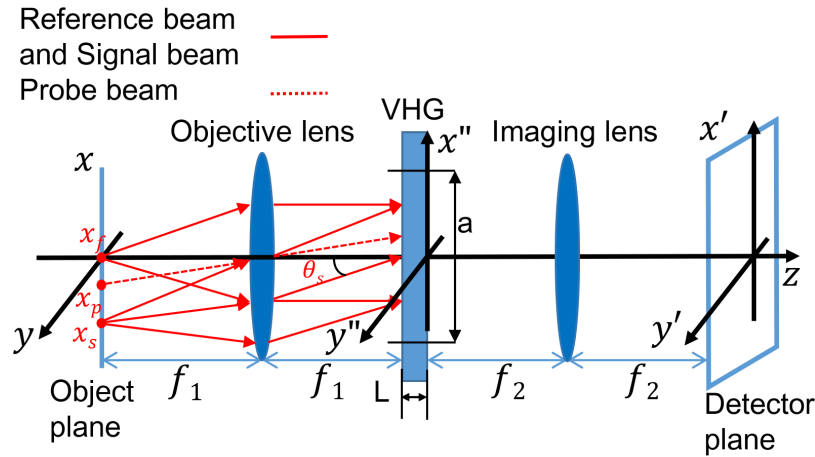
Fig. 2. Schematic layout of a standard VHI system, where f_1 and $f2$ are the focal lengths of the objective lens and imaging lens, respectively. a and L are the lateral aperture and thickness of the VHG respectively. x_f, x_s, and x_p represent the positions of the reference point source, signal point source and probe point source, respectively. θ_s is the inter-angle between the reference beam and signal beam.

where I_{max} is the maximum intensity of the bright fringes and I_{min} is the minimum intensity of the dark fringes in each region of interest (ROI).

This phenomenon has significant effect on the image contrast acquired by broadband VHI system and limits the application of the system in biomedical imaging fields that requires high image contrast of sample features. However, the reason of the horizontal blurring is different from the one for the degradation of depth selectivity previously discussed [7]. To simplify the analysis of the 3D Fourier filter under broadband illumination, we consider the light distribution on the detector plane $q(x', y')$ of the $4f$ VHI system containing a slab shaped VHG shown in Fig. 2, because the geometry is convenient and the impulse response $h(x', y'; x, y)$ and the system input-output relation under monochromatic illumination have been reported previously without missing the general Bragg properties of the 3D Fourier filter [15], as

$$
\begin{aligned}
h(x', y'; x, y) = & sinc \left[a \left(\frac{x}{\lambda_p f_1} + \frac{x'}{\lambda_p f_2} - \frac{x_s - x_f}{\lambda_f f_1} \right) \right] sinc \left[b \left(\frac{y}{\lambda_p f_1} + \frac{y'}{\lambda_p f_2} \right) \right] \\
& sinc \left[\frac{L}{2} \left(\frac{x^2 + y^2}{\lambda_p f_1{}^2} - \frac{x'^2 + y'^2}{\lambda_p f_2{}^2} + \frac{x_s{}^2 - y_f{}^2}{\lambda_f f_1{}^2} \right) \right],
\end{aligned}
\tag{3}
$$

and

$$
q(x', y') = \iint p(x, y) h(x', y'; x, y) dx dy,
\tag{4}
$$

respectively, where λ_p and λ_f are the are the probe wavelength and the recording wavelength of the VHG, respectively. $p(x, y)$ and $q(x', y')$ represent the light distribution on the object plane and the detector plane, respectively.

We now consider the simplest case, the $4f$ imaging system is probed by a point source $p(x, y)$, which is located in the vicinity of the reference point source $(x_f, 0, -f_1)$. For convenience, the lateral magnification of the $4f$ system is calculated as $m = f_1/f_2$, and the probe wavelengths are firstly normalized as

$$
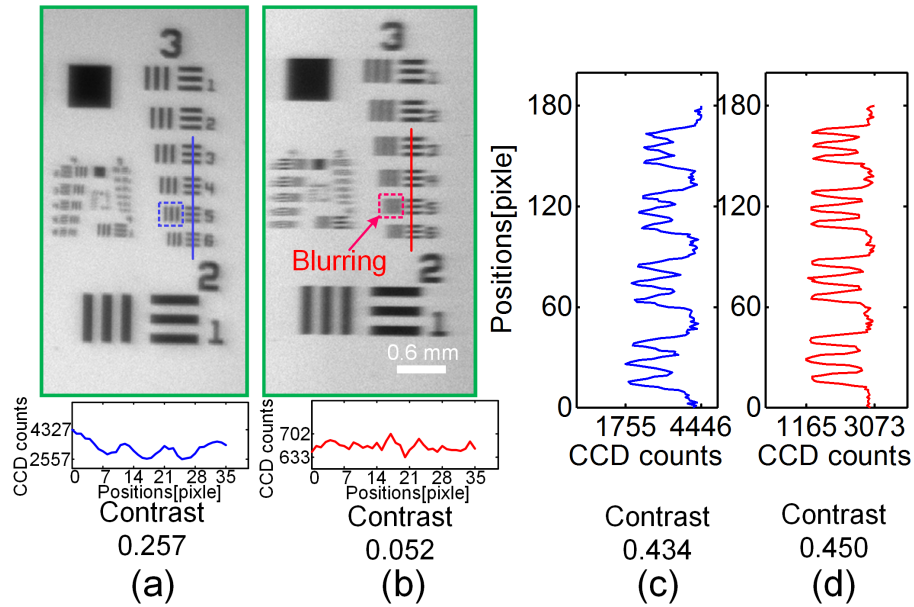\mu = \frac{\lambda_p}{\lambda_f},
\tag{5}
$$

Fig. 3. Experimentally characterized horizontal blurring in the broadband VHI. The USAF test target chart is focused and illuminated with transmission mode. (a) Image acquired without using the VHG. (b) Diffracted image acquired with the VHG placed on the Fourier plane. The horizontal contrast shows a significant reduction, while the vertical contrast is less affected. The average plots of Group 3 Class 5 marked with blue and red dashed rectangles are provided in (a) and (b). And (c) and (d) are the intensity profiles along the line perpendicular to the stripes in (a) and (b), respectively.

The point source emits two wavelengths, one at the recording wavelength $\mu = 1$ and the other deviating $\Delta\lambda$ from λ_f, i.e., $\mu = 1 + \Delta\mu$. Substituting Eqs. (3) and (5) into (4), we obtain

$$q(x', y') = sinc\left[a\frac{x' + \mu m x_s + m(x - \mu x_f)}{\lambda_p f_2}\right] sinc\left[b\frac{y' + my}{\lambda_p f_2}\right]$$
$$sinc\left[L\frac{(\mu m^2 x_s{}^2 - x'^2) + m^2(x^2 - \mu x_f{}^2)}{2\lambda_p f_2{}^2}\right], \tag{6}$$

The image positions of the Bragg matched wavelength $\mu = 1$ and the mismatched wavelength $\mu = 1 + \Delta\mu$ can be identified as Eqs. (7) and (8), respectively. The two equations show that although the two probe wavelengths originate from the same point, the image position of the mismatched wavelength deviates horizontally from the matched one.

$$x' = -\mu m x_s, \tag{7}$$

$$x' = -\mu m x_s - m\Delta\mu x_f, \tag{8}$$

Now we consider the broadband point source case, i.e., $\mu = [1 - \Delta\mu, 1 + \Delta\mu]$. The diffracted

intensity distribution of the broadband point source $p(x, y, \mu)$ can be calculated as

$$
\begin{aligned}
|q(x', y', \mu)|^2 &= \iint_{x,y} dx\,dy \int_{1-\Delta\mu}^{1+\Delta\mu} |p(x, y, \tau)|^2 |h(x', y'; x, y, \tau)|^2 d\tau, \\
&= \iint_{x,y} dx\,dy \int_{1-\Delta\mu}^{1+\Delta\mu} |p(x, y, \tau)|^2 sinc^2 \left[a \frac{x' + \tau m x_s + mx - m\tau x_f}{\lambda_p f_2} \right] \times \\
&\quad sinc^2 \left[b \frac{y' + my}{\lambda_p f_2} \right] sinc^2 \left[L \frac{(x_s^2 - x_f^2)\tau m^2 + (x^2 + y^2)m^2 - (x'^2 + y'^2))}{2\lambda_p f_2^2} \right] d\tau,
\end{aligned}
\tag{9}
$$

The image intensity of the broadband point source is not only the energy of the Bragg matched wavelength $\mu = 1$, but a weighted superposition of the energy of the adjacent wavelengths. The weighting factor of each mismatched wavelength depends on the diffraction efficiency and the spectrum profile of the source. The position deviations of the mismatched wavelengths lead to horizontal intensity spread. Therefore the images of the broadband point are horizontally blurred.

For further illustrate the horizontal intensity spread, the simulated and experimentally measured diffractive patterns of both monochromatic point source and broadband point source are shown in Fig. 4. In the simulation, a slab shaped hologram (clear aperture width 22 mm, thickness 1.8 mm) with Bragg matched wavelength at $\lambda = 530\ nm$ is utilized, and the spectral bandwidth of the broadband point source is 40 nm. For the parameters used in this simulation, the horizontal intensity spread with the broadband source is $3\times$ worse than the one with a monochromatic source. In the experiment, the $4f$ VHI consists of a self-recorded VHG (diameter $a = 22\ mm$, thickness $L = 1.8\ mm$), a focal length $f_1 = 100\ mm$ achromatic objective lens (AC-254-100-A, Thorlabs, NJ) and a focal length $f_2 = 75\ mm$ achromatic imaging lens (AC-254-075-A, Thorlabs, NJ). The The diffraction pattern of the monochromatic beam is acquired by probing the $4f$ VHI system with a 2.0-mm diameter collimated 488-nm laser beam (LWBL488-60, Laserwave, Beijing, China), and the main lobe is deliberately saturated to obtain clear side lobes. The operation of saturation caused the expansion of the main lobe area, which is larger than the diffraction pattern obtained under normal acquisition condition. The broadband point sources are acquired by illuminating a 25-μm diameter pinhole with Xenon lamp (MAX-302, ASAHI SPECTRA, Tokyo, Japan).

According to the above analysis, the horizontal contrast can be improved by using monochromatic illumination. However, this approach sacrifices the horizontal FOV, because the FOV along the horizontal direction is directly determined by the spectral bandwidth of the illumination and the angular selectivity of the VHG [16]. Therefore, the point-spread deconvolution method is proposed here to overcome the degradation of horizontal contrast problem brought by probing the VHG with broadband illumination.

3.2. The impulse response of broadband VHI

When the object is uniformly illuminated with a broadband point source, the intensity distribution on the image plane is determined by the position of each object point and the spectrum profile of the broadband illumination. Although the 3D Fourier filter exhibits shift variant property due to the angular-spectral selectivity, the impulse response of the $4f$ VHI system under broadband illumination with uniform spectrum profile can be dealt as intensity shift invariant. If the image point location shifts along the horizontal direction, the Bragg matched wavelength changes [2], but the variation of intensity distribution on the detector is inconspicuous. The diffraction patterns have the similar profile (Fig. 5(b)). The point sources with two different bandwidths are created by illuminating the 25 μm pinhole with 536 nm (with a full width at half maximum (FWHM) bandwidth of 40 nm) and 530 nm (with an FWHM bandwidth of 10 nm) light source. The diffractive intensity variation as the two point sources shift 2.0 mm along the horizontal direction
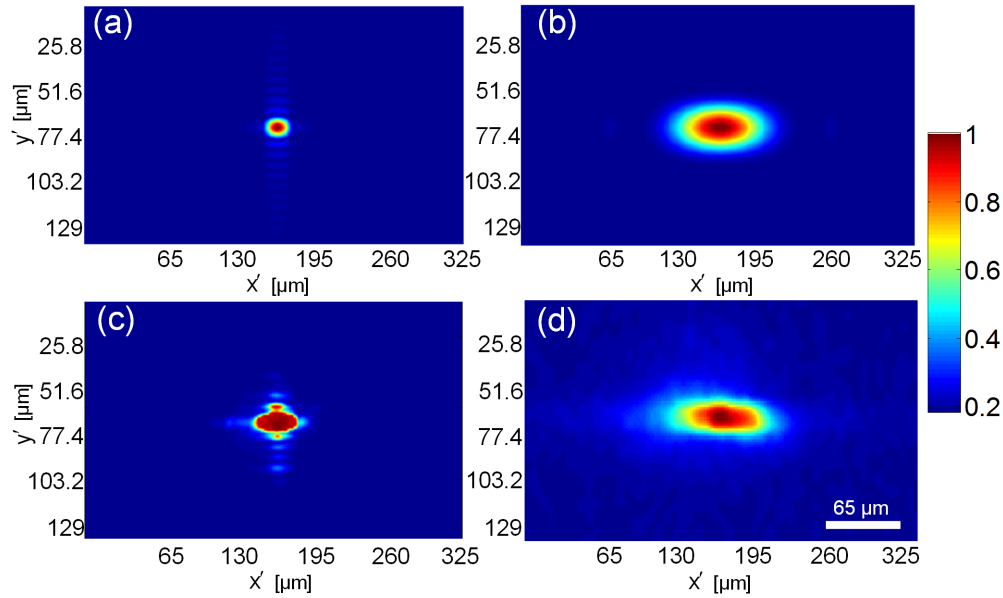
Fig. 4. The (a, b) simulation and (c, d) experimental measurements of probing a $4f$ VHI system with point source. Diffraction pattern of (a) monochromatic point source and (b) broadband point source. The simulation system consists a slab-shaped VHG with $a = 22\ mm$, $L = 1.8\ mm$, and the focal length of the objective lens and imaging lens are $f_1 = 100\ mm$ and $f_2 = 75\ mm$, respectively. The experimental results of probing a $4f$ VHI system with (c) collimated monochromatic laser beam and (d) white light point source, respectively. The slab-shaped VHG has a diameter $a = 22\ mm$, thickness $L = 1.8\ mm$, the focal lengths of objective lens and imaging lens are $f_1 = 100\ mm$ and $f_2 = 75\ mm$, respectively. The point source is created by illuminate a 25-μm pinhole with white light source. Each figure is normalized by its peak value.

are shown in Figs. 5(c) and (d). The coefficient of variation (CV) of diffraction intensity (defined as the standard deviation divided by the mean value) in Figs. 5(c) and (d) are calculated as 4.0% and 46.8%, respectively.

3.3. The discretized optical model

According to the above the analysis, the horizontal blurring of the image obtained by the broadband illuminated $4f$ VHI system can be modeled as a convolution between the object and the impulse response, which leads to the degradation of local contrast of the image. The observed image described with the general linear incoherent intensity integral

$$I_{img}(x', y', \mu) = \iint_{x,y} dxdy \int_{1-\Delta\mu}^{1+\Delta\mu} |g_{illum}(x, y, \tau)|^2 |h(x', y'; x, y, \tau)|^2 d\tau, \qquad (10)$$

An effective way to solve the blurring problem is the deconvolution approach. And the imaging process can be expressed by the discrete linear model,

$$\mathbf{b} = \mathbf{Ax} + \mathbf{e}, \qquad (11)$$

In Eq. (10), $I_{img}(x', y', \mu)$ represents the image intensity distribution on the detector, $|g_{illum}(\cdot)|^2$ represents the intensity distribution on the object plane and $h(\cdot)$ represents the
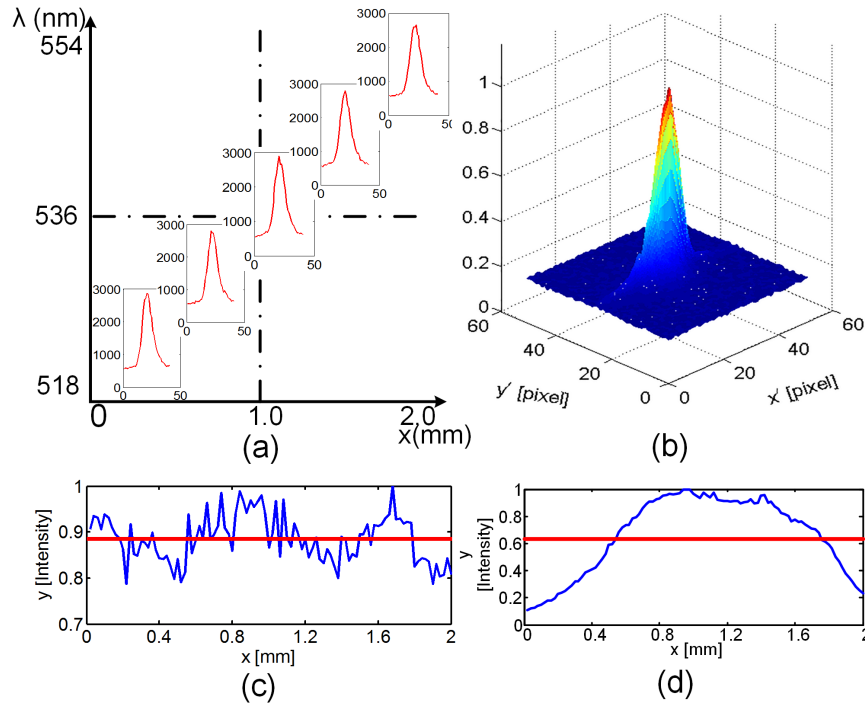
Fig. 5. Experimentally observed diffraction patterns along different horizontal positions. (a) The intensity profiles (marked with red line) when the $536 \pm 20\ nm$ (FWHM bandwidth $40\ nm$) point source passing through the peak of the main lobe. (b) The diffraction pattern of the $25\ \mu m$ point source uniformly illuminated with a $536 \pm 20\ nm$ broadband source. (c) and (d) are the diffraction intensity fluctuations (marked with blue lines) during the process of moving the $536 \pm 20\ nm$ and $530 \pm 5\ nm$ point source horizontally. The distance of the movement is $2.0\ mm$. And the coefficient of variation (CV) around the mean diffraction intensity (marked with red line) of the $536 \pm 20\ nm$ point source is within 4.0%, while the CV of the $530 \pm 5\ nm$ point source is larger than 46.8%.

impulse response of the imaging system. In Eq. (11), **b** represents the recorded blurred image vector, **A** represents the measurement matrix modeling the forward imaging process, **x** is the ideal image vector and **e** is the noise vector.

We now focus on seeking the solution of the discrete linear image blurring model. To complete the discrete model, the measurement matrix **A** is constructed by measuring a broadband point source at different positions of the FOV through the $4f$ VHI system. Its entries $a_{i,j}$ indicate the proportion of the energy arriving at pixel j from point i of the object, which is caused by the intensity horizontal spread effect. The columns of **A** contain the discrete version of forward projection generated when a non-zero object point is projected according to Eq. (10) [17]. In the consideration of practicality, we used one directly measured point spread function (PSF) of the VHI system for constructing the measurement matrix by making two assumptions about the imaging characteristic of the system and the thickness of the object. First, the intensity impulse response of the $4f$ system is invariant across the FOV under uniform broadband illumination. This assumption is reasonable according to the above analysis. Second, the object has small thickness, i.e., it is assumed that there is no scattering light originating from the deep layer of the object, because in broadband VHI, the image can also be affected by the energy from the out-of-focus points.

Due to the large size of the detector and the presence of additive noise, it is not reasonable to store a huge matrix in memory and perform deconvolution directly. Therefore, the truncated singular value decomposition (TSVD) approach is utilized solve this problem without explicitly constructing the measurement matrix, and a regularization parameter is introduced to mitigate the noise amplification [18].

$$x_{filt} = V\Sigma_{filt}^{-1}U^T b, \qquad (12)$$

where x_{filt} represents the reconstructed real image, V, Σ^{-1} and U^T are the singular matrices of $\mathbf{A}^{-1}$, $\Sigma_{filt}^{-1} = \Phi\Sigma^{-1}$ and Φ is the filter factor matrix.

4. Experimental results

In this Section, the experimental measurements processed with the aforementioned optical model and the deconvolution method are presented. Three different imaging experiments, including US-AF test target, biological tissue and fluorescent objects, are performed to illustrate the horizontal contrast improvement by using the proposed method. In the experiments, two complementary custom built imaging system were employed. The first one is a $4f$ VHI system constructed with two simple achromatic lenses (AC-254-100-A used as objective lens with 100 mm focal length and AC-254-075-A used as imaging lens with 75 mm focal length) and the self-recorded VHG (diameter $a = 22mm$, thickness $L = 1.8mm$) for imaging the USAF test target and biological tissue. The second one is a $4f$ VHI system constructed with a 20× plan field fluorescence objective lens (CFI S-Plan Fluor 20×, Nikon, Japan) and the achromatic lenses (AC-254-075-A, 75 mm focal length) used as the imaging lens for imaging the fluorescence microspheres.

4.1. Experimental characterization of contrast using USAF test target

In this experiment, a reflective USAF test target chart was utilized as an object for the comparison of the horizontal contrast between the blurred image and the reconstructed one. Figures. 6(a) and (b) are acquired when the target was uniformly illuminated with 536 ± 20 nm and 530 ± 5 nm broadband source in transmission mode, respectively. The relationship between the bandwidth and the lateral FOV is given by [8]:

$$FOV = \frac{B\theta_s f_{obj}}{\bar{\lambda}}, \qquad (13)$$

where $\bar{\lambda}$ is the mean wavelength of the broadband source, B is the source bandwidth, θ_s is the angle between the signal beam and the reference beam, and f_{obj} is the focal length of the objective lens. The simulation of the bandwidth (x axis) and FOV (y axis) are shown in Fig. 6(c). Figure 6(d) is the blurred USAF test target image. The horizontal contrast suffers from the intensity spread and the horizontal bars cannot be well resolved in Group 3 Class 5 (12.70 lp/mm), although the vertical bars is clear to be seen. After the deconvolution process (Fig. 6(e)), the lost details are retrieved in the reconstructed image. The local contrast in Group 3 Class 5 is improved by > 3.0×, and even the smallest horizontal features in Group 3 Class 6 (14.30 lp/mm) can be distinguished. Although the contrast of the reconstructed image still degrades with the decrease of line width, it is higher than that of the blurred one (Fig. 7).

4.2. Experiment on biological specimen

A hematoxylin and eosin (H&E) stained lung tissue section, obtained from an eight-week nude mouse, was used to demonstrate the feasibility and performance of the proposed method in the horizontal contrast improvement. In Fig. 8, the ground truth image, the degraded original image and the corresponding reconstruction results are all depicted. The ground truth image was acquired with the same system parameter without using the VHG. The comparison shows
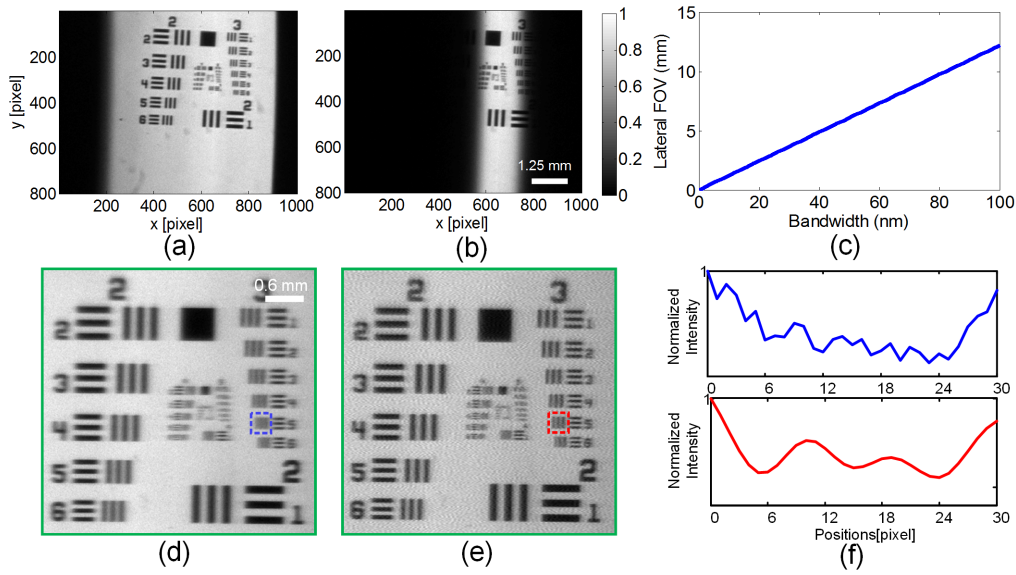
Fig. 6. Images of the USAF test target captured by a standard broadband $4f$ VHI system. (a) and (b) are the images when the target is illuminate with $536 \pm 20\ nm$ and $530 \pm 5\ nm$ source in transmission mode, respectively. (c) The relationship between the lateral FOV and the bandwidth. (e) Image after deconvolution of (d) image acquired by broadband VHI system with the aforementioned optical model. The average plots of Group 3 Class 5 in (d) and (e) (marked with blue and red dashed rectangles, respectively) in (f) show that the image contrast is significantly improved.
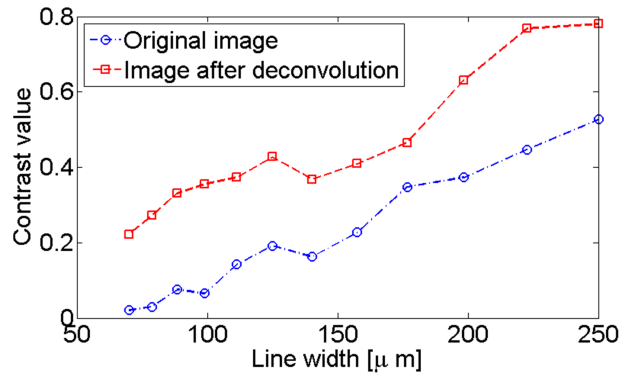

Fig. 7. Horizontal contrast comparison of the USAF test target at regions with different line widths. In each region, the image contrast is significantly alleviated by using the deconvolution method.

that the deconvolution method is capable of recovering more details (marked with red circles in Fig. 8) of the real tissue than the blurred image, however, some artifacts are also introduced. In order to quantitatively evaluate the quality improvement in the reconstructed image, the peak signal-to-noise ratio (PSNR) values are calculated as

$$PSNR = 10 \times log_{10}\left[\frac{(2^n - 1)^2}{MSE}\right], \tag{14}$$

where MSE is the mean square error between the ground truth image and target image. The PSNR of the reconstructed image are 67.48 dB, while that of the original blurred image is 67.35 dB. In the reconstructed image, there are some visible freckles with high spatial frequencies in the background, which can degrade the PSNR of the reconstructed imaged. However, it could be alleviated by introducing other smoothing *p-norms* with *p* close to 1 [19].
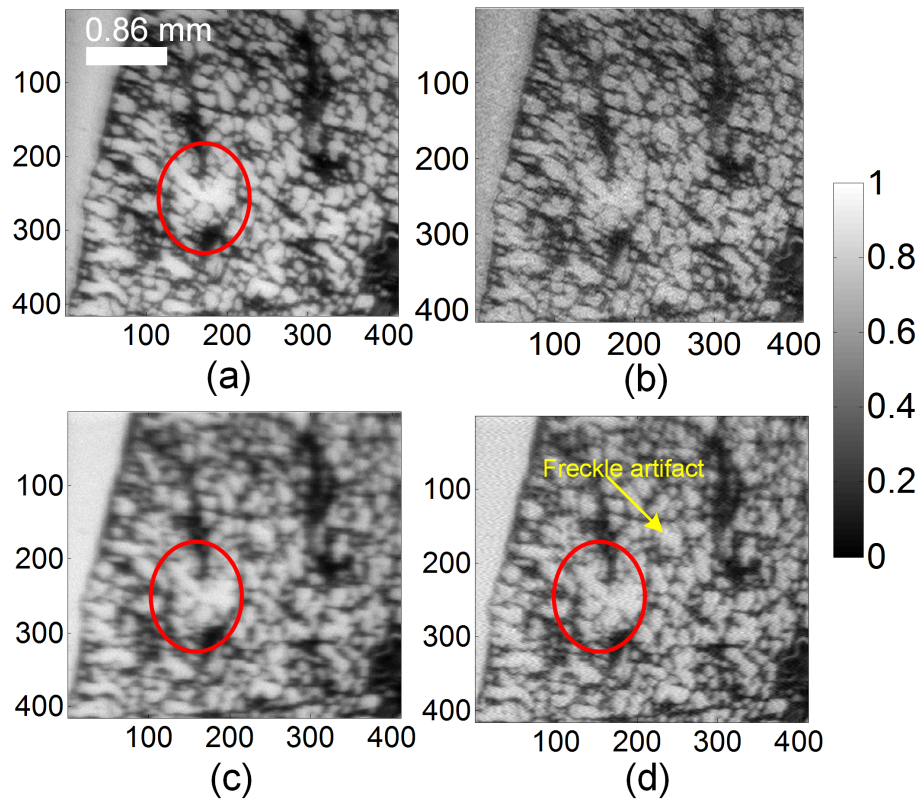

Fig. 8. Images of broadband illuminated (536 ± 20 *nm*) lung tissue section, obtained from an eigth-week nude mouse. (a) The broadband illuminated image acquired by the $4f$ VHI system without using the VHG. (b) The deconvolution results of (a) with PSF acquired with the 4f VHI system without VHG. (c) The diffraction image acquired with the VHG placed on the Fourier plane of the 4f VHI system, and (d) the reconstructed image with the deconvolution method. The unit of these images in both the vertical and horizontal directions is the size of CCD pixel (6.45 μm in width).

4.3. Experiment on fluorescent beads

In biomedical imaging applications, bandpass filters is widely used to block excitation light from fluorescence signals. Because of the intensity spread effect of VHI system under broadband illuminations, the degradation of horizontal contrast also exists in fluorescence VHI applications. And this effect can hamper the application of VHI system in some high standard biomedical imaging areas. In this experiment, two adjacent fluorescent microspheres were excited with a 488 *nm* laser (LWBL488-60, Laserwave, Beijing, China) and a 500 *nm* long-pass fluorescence filter (FELH0500, Thorlabs, NJ) was used to block out the excitation light. The FWHM bandwidth of the fluorescence emitted by the fluorescent microspheres was measured as 37 nm. To acquire the

impulse response of this system, a 5-μm diameter pinhole illuminated with white light was used to create the point source. The fluorescence images of 15-μm diameter microspheres (F-21012, Invitrogen, Carlsbad, CA) are shown in Fig. 9.

Figure. 9(b) is the reconstruction result of the ground truth image, and the details of the two beads in the image are improved. However, the background noise is amplified. As shown in Fig. 9(d), the horizontal intensity spread is alleviated, and the details of the objects are well distinguished. There are some visible ring artifacts around the microspheres, and this problem can be mitigated by using smaller pinholes and more effective smoothing filter or compressive sense algorithms [20].
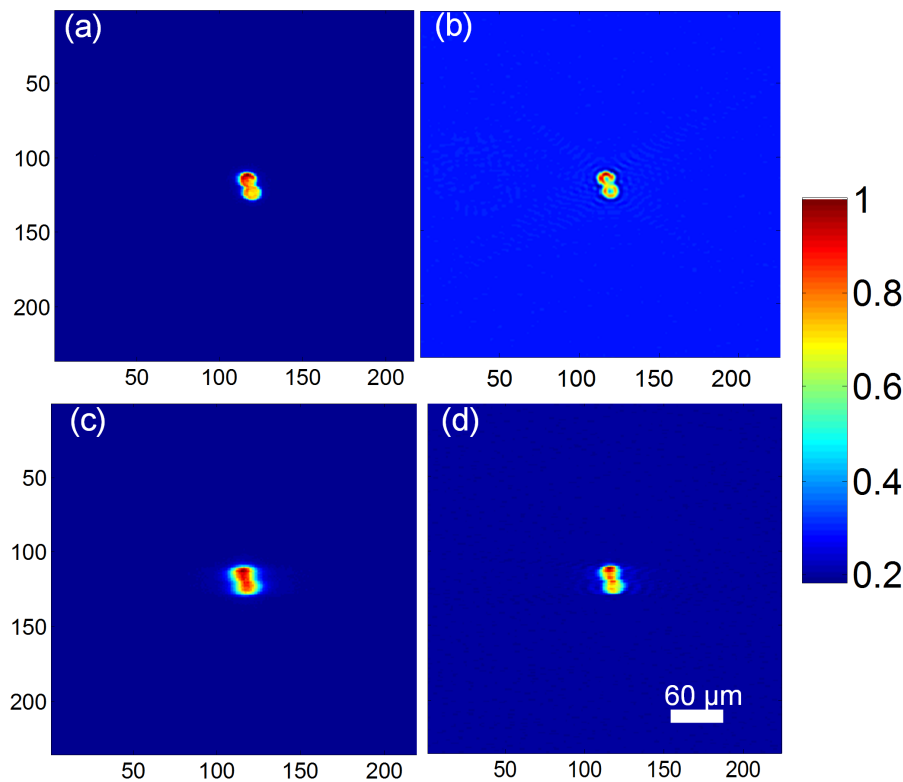

Fig. 9. The images of two adjacent 15 μm fluorescence beads. (a) The ground truth image acquired with the $4f$ VHI system without using the VHG. (b) The reconstructed rersult of (a) with the PSF acquired without using VHG. (c) The image acquired with the VHG on the Fourier plane of the 4f VHI system. (d) The reconstructed image of the two microspheres.

5. Discussion and conclusion

In order to obtain an optimized structure of the $4f$ VHI system and meet the requirements of broadband imaging applications, the relationship between the intensity spread and the system structure parameters should be examined further.

The intensity spread in the horizontal direction mainly depends on the structure parameters of the $4f$ imaging system, such as the focal length of the objective lens f_1, magnification of the $4f$ system m, the angular-selectivity $\Delta\mu$ of the VHG and the spectral bandwidth of the probe source. When the $4f$ VHI system is illuminated by a broadband point source located at the focus, the extent of horizontal intensity spread on the image plane is determined by the angularity

selectivity $\Delta\mu$ of the prerecorded VHG [15]. The locations of the Bragg mismatched wavelength deviated $\Delta\mu$ from the Bragg matched wavelength λ_f on the detector plane can be expressed as

$$\Delta x' = -m\frac{2\lambda_f}{L}\frac{f_1}{\theta_s}, \tag{15}$$

where L and θ_s are the thickness and Bragg matched angle of the prerecorded VHG, respectively, λ_f is the Bragg matched wavelength. Figure. 10(a) shows that the degree of intensity spread increases with the increase of the focal length of the objective lens and the lateral magnification m. For a fixed magnification factor m, the use of an objective lens with short focal length can effectively reduce the extent of the spread effect. When the structure parameters of the $4f$ system is determined, a thicker VHG is preferred for the broadband VHI applications.
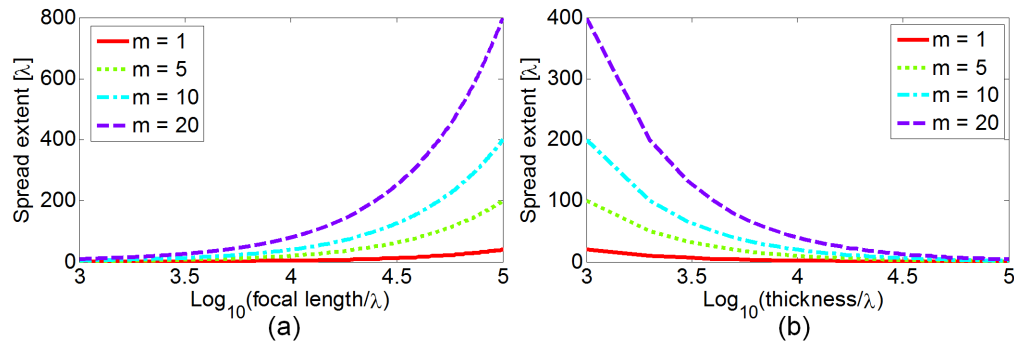

Fig. 10. The extent of horizontal intensity spread as a function of the focal length of objective lens and the thickness of prerecorded VHG. (a) For a fixed magnification factor m, longer focal length results in larger spread extent. (b) For a fixed $4f$ system structure, increased thickness of the VHG results in better performance in suppressing the horizontal intensity spread.

In this paper we presented the theoretical and experimental analysis for horizontal blurring of broadband VHI, and we showed that with the image contrast can be improved without sacrificing the horizontal FOV by narrowing down the illumination bandwidth or constructing additional illumination structures. To determine the diffraction intensity distribution on the detector plane, we simulated and measured the impulse response of the 3D VHG Fourier filter under broadband illumination as it impacts the imaging performance of the VHI system. We explained the reason why the deconvolution method can be used to improve the horizontal contrast of the images acquired by the $4f$ VHI system under broadband illumination. Then three imaging experiments including bright-field and fluorescence imaging were conducted to illustrate the improvement of the image contrast in the horizontal direction. The results showed that the deconvolution method provides a flexible approach to improve the horizontal contrast of fluorescence image. And this approach can be applied to simultaneous multi-depth and multispectral VHI. The simulation of the relationship between the spread extent and the $4f$ VHI system parameters are also provided, which can help to configure the $4f$ VHI system for various biomedical imaging applications.

Ideally, to perform deconvolution, both the original image and the PSF should be free of aberration. However, although the lenses used in the experimental system are all achromatic to minimize the effect of axial aberrations, it is inevitable to confront axial aberrations in the broadband imaging. To eliminate aberrations with deconvolution method, the PSF must be selected appropriately to match the aberrations that appear in the original images. And the performance of this procedure essentially depends on empirical practice [21]. In this work, the deconvolution approach was applied by directly measuring the broadband system impulse

response and assuming similar impulse response across the FOV. However, this assumption may not be fulfilled in real experiments and this can affect the performance of the deconvolution method. This limitation might be circumvented by modeling the broadband impulse response across the FOV or adopting the blind image deblurring methods [22]. And further studies need to be carried out to quantitatively access the performance of the deconvolution method in correcting the axial aberrations of broadband VHI.

Acknowledgments